Upward transport and segregation of ice-nucleating particles in deep convective clouds

Jonas Schaefer[a], Sarah Grawe[a], Hans-Christian Clemen[b], Stephan Mertes[a], Johannes Schneider[b], Bruno Wetzel[a], Daniel Sauer[c], Jennifer Wolf[c], Laura Tomsche[c,d], Johanna Mayer[c], Roland Schrödner[a], Silvia Henning[a], Tina Jurkat-Witschas[c], Christiane Voigt[c,d], Helmut Ziereis[c], Theresa Harlaß[c], Mira Pöhlker[a,e], and Frank Stratmann[a]

[a]Leibniz Institute for Tropospheric Research TROPOS, Leipzig, Germany
[b]Aerosol Chemistry Department, Max Planck Institute for Chemistry, Mainz, Germany
[c]Deutsches Zentrum für Luft- und Raumfahrt (DLR), Oberpfaffenhofen, Germany
[d]Johannes Gutenberg-Universität Mainz, Mainz, Germany
[e]Leipziger Institut für Meteorologie (LIM), Universität Leipzig, Leipzig, Germany

Correspondence: Jonas Schaefer (jschaefer@tropos.de)

Abstract. Ice-nucleating particles (INPs) play a crucial role in Earth's weather and climate by influencing cloud properties and precipitation. However, their abundance in the free troposphere, vertical distribution, and transport mechanisms are not well-characterized. This study presents immersion INP measurements from filter samples collected aboard the High Altitude and LOng range research aircraft (HALO) in the troposphere and the lower stratosphere (up to 14.5 km) over Europe during the CIRRUS-HL (Cirrus in High Latitudes) campaign in summer 2021. By sampling cloud particle residuals and aerosol particles in the inflow and outflow of deep convective clouds (DCCs), and performing offline INP analysis, we shed light on the vertical transport and segregation of INPs in DCCs.

INP-temperature spectra of convective inflow included both INPs active at high (T > -15 °C) and low temperatures (T < -20 °C). In contrast the outflow spectra only featured INPs active at low temperatures. We explain the observed INP segregation in the updraft with precipitation scavenging of INPs active at high temperatures. INPs active at lower temperatures (T < -20 °C), however, are efficiently transported upwards into the free troposphere. There, ambient temperatures are below -40 °C, i.e., temperatures far below the temperatures at which these INPs initiate immersion freezing. In the DCC outflow, INP concentrations exceed the upper tropospheric background concentration by at least two orders of magnitude. These INPs are then available for ice formation in mid and upper tropospheric clouds.

1 Introduction

Clouds are a key factor in the Earth's climate system. The microphysical properties of clouds, such as their phase state, determine their effects on radiation and the formation of precipitation (Tan et al., 2016). For instance, liquid clouds typically consist of numerous small droplets, rendering them optically thick. In contrast, ice clouds often contain fewer large ice crystals in the same volume and reflect short-wave radiation less effectively (Storelvmo, 2017). Worldwide, precipitation is predominantly formed in ice-containing clouds (Mülmenstädt et al., 2015). In cloud droplets which lack ice-nucleating particles (INPs) as catalyst, ice nucleates at a temperature of around -38 °C. This process is called homogeneous freezing. Between 0 °C and -38 °C, ice crystals form in the presence of INPs, i.e., through heterogeneous nucleation. With decreasing temperature, the number of aerosol particles acting as INP increases exponentially, making them a key factor determining the phase state of clouds. When ice crystals and water droplets coexist, they form mixed-phase clouds, which cover vast areas of the Earth's surface (Choi et al., 2010; Mayer et al., 2024). The dominant freezing mechanism within mixed-phase clouds is immersion freezing (Ansmann et al., 2009), i.e., heterogeneous freezing of supercooled droplets induced by immersed INPs.

While many studies examined and characterized INPs at ground level and inside the atmospheric boundary layer, few investigated INPs within the free troposphere (FT), extending from the top of the boundary layer to the tropopause. Limited measurements conducted on aircraft (Barry et al., 2021; Levin et al., 2019; Twohy et al., 2021; Moore et al., 2024) and atop tall mountains (Conen et al., 2022; Brunner et al., 2022) hint at generally lower INP concentrations in the free troposphere compared to results from ground-based measurements. Across several campaigns, free tropospheric background concentrations of INPs active at -30 °C (effective temperature, T_{eff}), have been found to be below $10\,\text{sl}^{-1}$ (standard liter, p = 1013 hPa, T = 0 °C; Lacher et al., 2018). Recent studies showed higher FT INP concentrations in spring and summer, indicating a seasonal variability (Brunner et al., 2022). FT concentrations of INP nucleating ice below T_{eff} = -15 °C were found to increase during desert dust advection events (Lacher et al., 2018, 2021; Brunner et al., 2022). Above -15 °C, bacteria and fungal spores, and fragments of those, represent the majority of FT INPs (Conen et al., 2022). Furthermore, sea salt aerosol particles, incorporating marine organics, correlate with FT INP concentration and have been identified within ice crystal residuals (Lacher et al., 2021). In regions with scarce mineral dust, these marine organics may dominate the FT INP population active above -20 °C (Vergara-Temprado et al., 2017; McCluskey et al., 2023).

Overall, FT INPs originate at ground level, making investigation of vertical transport mechanisms that lift INPs from the ground into the FT a crucial task. One such mechanism is orographic lifting in mountainous regions, which can transport INPs upward on a smaller scale (Wieder et al., 2022). Uplift in deep convective clouds (DCCs) is a pathway through which large amounts of aerosol particles are transported from the boundary layer into the upper troposphere (Yin et al., 2012; Yang et al., 2015). However, the importance of DCCs as upward transport mechanism for INPs is currently unclear. Many studies investigated the sensitivity of DCC characteristics with respect to variations in INP concentrations (Hiron and Flossmann, 2015; Gibbons et al., 2018; Takeishi and Storelvmo, 2018; Diehl and Grützun, 2018; Hawker et al., 2021b, a). However, the effects of clouds on INPs, including their upward transport and potential depletion by wet removal in precipitating clouds (Stopelli et al., 2015; Pouzet et al., 2017; Els et al., 2019), add a currently not sufficiently understood layer of complexity to the interactions between INPs and clouds (Burrows et al., 2022). This study aims to elucidate these processes with a novel instrument for aircraft application.

The High Altitude and LOng Range research aircraft (HALO) serves as an ideal platform for investigating free tropospheric and lower stratospheric INPs, in general, and the vertical transport and cloud processing of INPs, in particular. Stationed in Oberpfaffenhofen (Germany) during June/July 2021, the Cirrus in High Latitudes (CIRRUS-HL) campaign aimed at the investigation of cirrus clouds in high-latitudes and above central Europe, with both in-situ and remote sensing instruments being operated over the course of 24 research flights (Jurkat-Witschas et al., 2025). In addition to focusing on cirrus clouds, the weather conditions during the campaign allowed for several research flights in and around DCCs. The effects of vertical transport and cloud processing on INPs were investigated by probing DCC inflow aerosol particles, cloud particle residuals (CPR), and upper tropospheric convective outflow aerosol particles in quick succession. To quantify the abundance and properties of atmospheric high-temperature INPs, the high-volume flow aerosol particle filter sampler (HERA, Grawe et al., 2023) was used for the first time on HALO during the CIRRUS-HL mission. The collected filters were later analyzed for INP activity. In addition to aerosol sampling, operating HERA at the counter flow virtual impactor inlet (HALO-CVI) allowed for sampling and analysis of CPRs, offering additional information on potential INPs immersed in cloud particles. Such an analysis for INPs in upper tropospheric CPRs are scarce until now (Cziczo et al., 2004; Eidhammer et al., 2010; Levin et al., 2019; Moore et al., 2024).

In conjunction with particle sampling by HERA, simultaneous measurements of the chemical composition of aerosol particles and cloud particle residuals by single particle mass spectrometry and further particle properties, such as number size distribution (Voigt et al., 2022), were carried out. These measurements are used to chemically characterize the prevailing aerosol particles and to identify their potential sources. It is not possible to draw conclusions concerning the chemical composition of the INPs present due to their low number concentration fraction. To the best of our knowledge, the present study represents the first comprehensive experimental investigation of INP transport and processing in DCCs. With that, it contributes greatly to our understanding of INP vertical transport and the influence of in-cloud processes on the INP population.

2 Methods

2.1 Aerosol- and cloud particle residual sampling

During the HALO Aircraft campaign CIRRUS-HL (Jurkat-Witschas et al., 2025), aerosol particles were sampled through an aerosol inlet. The filter sampler HERA (Grawe et al., 2023), used for INP sampling, was connected to that inlet together with two other instruments measuring single-particle chemical composition (ALABAMA, Brands et al., 2011; Clemen et al., 2020) and the aerosol particle number size distribution, respectively. The latter was carried out using two optical particle counters (both GRIMM Sky-OPC, model 1.129; Bundke et al., 2015), one connected to the aerosol inlet at all times and another switched to the HALO-CVI (see section below) along with ALABAMA during in-cloud measurements. The relative humidity in the sampling line remained below 50 % throughout the flights.

Ground-based measurements of INPs have shown that supermicron aerosol particles contribute substantially to INPs active at temperature above -25 °C (Mason et al., 2016). The aircraft aerosol inlet is a modified version of the HALO submicrometer inlet (HASI). It was adapted from a previous setup featuring multiple sampling lines (Andreae et al., 2018) to a single sampling line supplying all instruments to facilitate sampling of supermicron aerosol particles (Grawe et al., 2023) with a total flow rate of up to $80\,\mathrm{l\,min^{-1}}$.

Transmission losses were determined using the Particle Loss Calculator (Von der Weiden et al., 2009) and have been presented for the CIRRUS-HL setup of HERA in Grawe et al. (2023). In summary, for HERA operating at the HASI inlet with $40\,\mathrm{l\,min^{-1}}$ sample flow rate, an upper cutoff particle diameter d_{50} of 2.7 µm was determined assuming spherical particles with a density of $2\,\mathrm{g\,cm^{-3}}$ and typical sampling conditions, i.e., an inline pressure of $340\,\mathrm{hPa}$ at $200\,\mathrm{m\,s^{-1}}$ true air speed. For the ALABAMA, an upper cutoff particle diameter d_{50} of $3.1\,\mathrm{\mu m}$ was calculated for operation at the HASI.

In order to investigate CPRs, hydrometeors were collected by a counter-flow virtual impactor (CVI) (Ogren et al., 1985). One significant improvement to previous HALO missions (Voigt et al., 2017) was the mounting position of HALO-CVI on the lower fuselage. At this position, cloud particle enrichment and shadow effects due to the airplane body are significantly reduced compared to sampling at the upper fuselage (Jurkat-Witschas et al., 2025). The size range of cirrus ice particles, whose CPRs were investigated, was between 5 and $60\,\mathrm{\mu m}$. The calculated transmission efficiency yielded d_{50} of $4.7\,\mathrm{\mu m}$ between the inlet and the HALO-CVI flow distribution in the cabin. The cut-off diameter is further reduced for instruments, which had rather long sampling lines to the flow distribution, resulting in d_{50} of $2.2\,\mathrm{\mu m}$ and $1.6\,\mathrm{\mu m}$ for HERA (with $5\ \mathrm{l\,min^{-1}}$ sample flow rate) and ALABAMA, respectively. HERA, ALABAMA and one of the Sky-OPCs were switched from HASI to the HALO-CVI as soon as clouds were encountered, if not otherwise specified.

2.2 INP sampling

HERA is an aerosol particle filter sampler designed for aircraft applications including the collection of airborne INPs. A detailed description and characterization of the instrument is given in Grawe et al. (2023). It features a revolver-like set of six filter holders, through which the sample flow is guided by a ball valve. During CIRRUS-HL, electrically driven valves connected HERA to the sampling line of either the HASI or the HALO-CVI. The volumetric sample flow rate of HERA was regulated to $40\,\mathrm{l\,min^{-1}}$ when connected to the HASI and to $5\,\mathrm{l\,min^{-1}}$ when connected to the HALO-CVI.

Aerosol particles were collected through the HASI on 0.8 µm polycarbonate filters (Nuclepore™ Track-Etched Membranes, UK), which are suited for INP sampling at high flow rates (Grawe et al., 2023; Lacher et al., 2023). For cloud particle residuals sampled through the HALO-CVI, $0.1\,\mathrm{\mu m}$ or $0.2\,\mathrm{\mu m}$ filters were used instead. This was done solely to generate a larger flow resistance, which was mandatory to precisely adjust low flow rates with the HERA pumps. Previous studies showed no systematic differences in collected INPs between 0.1 µm, $0.2\,\mathrm{\mu m}$ and 0.8 µm pore sizes (Grawe et al., 2023; Lacher et al., 2023). When no filter was sampled, the sample flow was either guided through the bypass of HERA or the valves at the inlet of HERA were closed and the sample flow was turned off.

The sampling strategy during CIRRUS-HL focused on capturing differences in INP concentration in contrasting environments, e.g. stratosphere vs troposphere, free troposphere vs boundary layer, high-latitude upper troposphere and lower stratosphere (UTLS) vs mid-latitude UTLS. At the same time, sampling volume was maximized in order to collect as many INPs as possible, yielding a representative dataset that is distinguishable from the method-inherent interference background (Li et al., 2022; Grawe et al., 2023, see SI 1.2 for details). On each research flight, at least one of the six filters was reserved as a flight blank, i.e., it was treated identically to the sampled filters but without exposure to a sample flow. These blank samples were used to determine the INP interference background. All inserted filters were extracted from HERA immediately after the flight or early on the following day. During the last five flight days, i.e., from research flights F18/19 (19th July) to F24 (29th July), only one filter was sampled per flight and all five (plus one blank filter) were extracted after the last campaign flight. The corresponding blank filter showed no sign of contamination. Filters were extracted in clean conditions in the hangar laboratory adhering to the protocol described by Barry et al. (2021), stored at -20 °C and shipped to Leipzig for offline INP analysis.

To support the interpretation of INP on the sampled filters the cumulative sampled particle fraction is ($CSPF$) is used to express the fraction of large aerosol (or cloud-residual) particles captured on the filter. We set the lower size limit to 500,nm, motivated by the broad correlation between number concentrations of particles larger than 500,nm and INP concentrations reported by DeMott et al. (2010). $CSPF$ was calculated according to Eq.1 where $\dot{m}$ is the HERA sampling mass-flow rate and n_{500} the number concentration for particles > 500 nm as measured by one of the optical particle counters mentioned above (Sec.2.1).

$$CSPF = \frac{\sum_{t=0}^{t} n_{500} \cdot \dot{m}}{\sum_{t=0}^{t_{end}} n_{500} \cdot \dot{m}} \tag{1}$$

2.3 Offline INP analysis

The offline INP analysis of the CIRRUS-HL filters has been described previously (Grawe et al., 2023). In short, filters were washed off with 3 ml of ultra-pure water, analyzed in two different cold stages to cover a broad range of INP concentrations between -10 °C and -30 °C. The cold stages Leipzig Ice Nucleation Array (LINA) and Ice Nucleation Droplet Array (INDA), have been described in detail in Chen et al. (2018) and Hartmann et al. (2019). INP concentrations were calculated from the measured frozen droplet fractions, using the formulae of Vali (1971), (Eq.S1). The calculation of confidence bands and the merging of LINA and INDA results was achieved by Monte-Carlo simulations according to Vali (2019). In addition, an interference background subtraction was applied (see SI 1.4 for more details).

2.4 Single-particle mass spectrometry

The Aircraft-based Laser ABlation Aerosol MAss spectrometer (ALABAMA, Brands et al., 2011; Clemen et al., 2020) was used to analyze individual particles in the size range from 230 nm to 3000 nm (50 % cutoff diameter with respect to detection efficiency) for their chemical composition and their vacuum aerodynamic diameter. The laser ablation ionization method used in the ALABAMA enables the identification of a wide variety of organic and inorganic substances (including heat-resistant substances such as metals, minerals and soot), as well as the internal mixing states of individual particles. For the analysis, the recorded mass spectra were grouped into clusters based on similarity, and the ion signals of the resulting clusters were used to identify particle types (for further details see: Roth et al., 2016; Schmidt et al., 2017; Lacher et al., 2021). A total of 10 particle types were identified during the CIRRUS-HL mission, which make up the majority of the composition of the aerosol particle and CPR population, albeit to different degrees. No correction was applied to the particle type fractions from the ALABAMA with respect to the size-dependent transmission losses calculated with the Particle Loss Calculator, since neither information on the density nor on the shape of the particles was available. However, a particle with the assumed diameter of 1.6 µm, a density of 2 g cm^{-3} and a shape factor of 1 is already at the upper end of the ALABAMA detection range with a vacuum aerodynamic diameter of 3.2 µm. An optical particle counter (GRIMM Sky-OPC, model 1.129), which is permanently integrated in the ALABAMA rack, records the particle size distribution above 0.25 µm.

3 Results and discussion

3.1 UTLS background INP concentrations during CIRRUS-HL

Of a total of 28 aerosol INP samples collected over 15 flight days, a subset of 12 samples meet the following criteria, which we consider representative of the UTLS background: no extended sampling in clouds (cloud sampling time <1.5 % of total sampling time per sample), no sampling in convective outflow regions, and no sampling within the atmospheric boundary layer. Furthermore, INP samples collected near warm conveyor belts were excluded using backward trajectories (De La Torre Castro et al., 2023; see 2.1 for further details). Samples collected in biomass burning aerosol (BBA) plumes were treated as UTLS background samples, due to their widespread presence in the central European UTLS in summer 2021 and the inefficiency of BBA particles to act as immersion INPs (Jurkat-Witschas et al., 2025).

A list of all selected UTLS INP samples is given in Tab. S1. Furthermore, a detailed description of sampling conditions is provided. In short, the combined sampling volume of all UTLS INP background samples is 20.2 m^3 and the sampling altitude ranged between 5 km and 15 km at ambient temperatures from 0 to -65 °C (see Fig. S7). As the campaign's focus was on cirrus rather than mixed-phase clouds, 94% of the air volume was collected at ambient temperatures below -35 °C (De La Torre Castro et al., 2023). Consequently, this dataset comprises background INP concentrations primarily obtained above the mixed-phase cloud level in terms of altitude.

Combining all UTLS INP concentrations into one dataset yields temperature-dependent probability density functions that roughly follow logarithmic normal distributions (see 2.2), consistent with Schrod et al. (2020). Weighted fitting of the dataset's medians (similar to Li et al., 2022, see 2.3 for details) between -15 °C and -27 °C with an exponential curve (Eq.2) yields a parameterization regarding background concentrations of INPs in the summer European UTLS, which can be applied in atmospheric models.

$$N_{\mathrm{INP}} = \exp\left(-0.5465\,°\mathrm{C} \cdot T[°\mathrm{C}] - 14.6199\right) \tag{2}$$

As can be seen in Fig. 1, UTLS INP background concentrations encountered during CIRRUS-HL are at the lower end of typical mid-latitude INP concentrations, which were determined from precipitation samples (gray area Fig. 1, Petters and Wright, 2015). Previous measurements of FT background INP concentrations in mid-latitudes at -30 °C (Lacher et al., 2018) align with the fit (pink line in Fig.1), despite their lower sampling altitude.

To characterize the overall UTLS background aerosol particle population and with that potential sources for INPs, prevailing particle types were analyzed by single-particle mass spectrometry and are shown in Fig. 2. The UTLS particle population comprised three main groups: 36 % contained mainly ammonium compounds, potassium compounds, and organics; 26 % were identified as BBA particles; and 31 % contained meteoric material. The fraction of the latter generally increases in the strato-

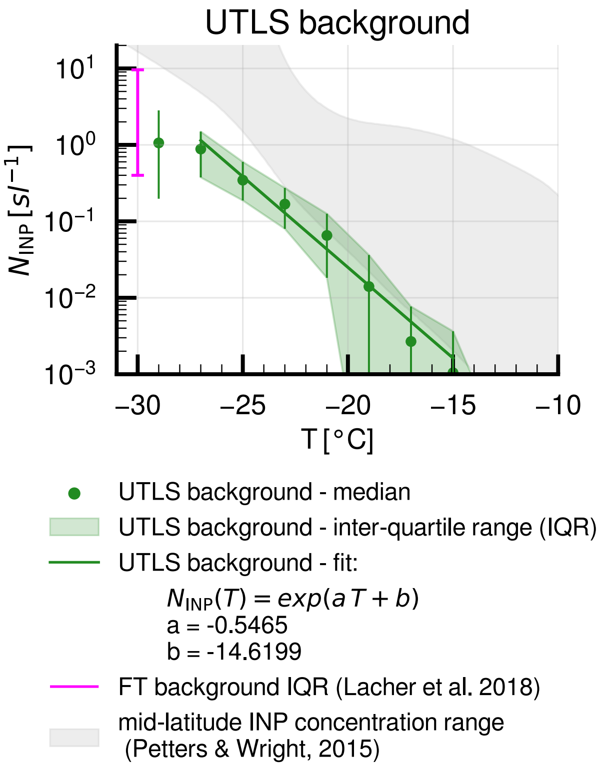

Figure 1. UTLS background INP concentration of CIRRUS-HL. Medians are marked with green dots, the inter-quartile range (IQR) is shown the green shaded area and the gray area marks typical mid-latitude INP concentrations (Petters and Wright, 2015). The pink error bar marks free tropospheric concentrations by Lacher et al. (2018).

sphere with altitude (Murphy et al., 2014; Schneider et al., 2021). Only 2.4 % of particles were identified as mineral dust/metal types and merely 0.3 % of particles are characterized as sea spray type. With this, the UTLS background is dominated by aged aerosol particles, which have been emitted directly (primary aerosol particles), and/or particles formed through gas to particle conversion (secondary aerosol particles). Unfortunately, the proportion of INP in the total number of aerosol particles is too low for establishing a robust link between INPs and specific particle types.

3.2 Deep convective cloud case study

3.2.1 Flight track

We investigated the influence of DCCs on the distribution and properties of INPs in the UTLS by analyzing the results of the measurements carried out during Flight 15 (F15). Figure 3 shows the HALO flight track of F15, on 13 July 2021. After takeoff in Oberpfaffenhofen, HALO moved NE and then southward over Austria into Italy. Following a turn towards SW, HALO descended on its way to Brescia airport, where a dive was performed. Shortly after, the plane moved N and then E, performing

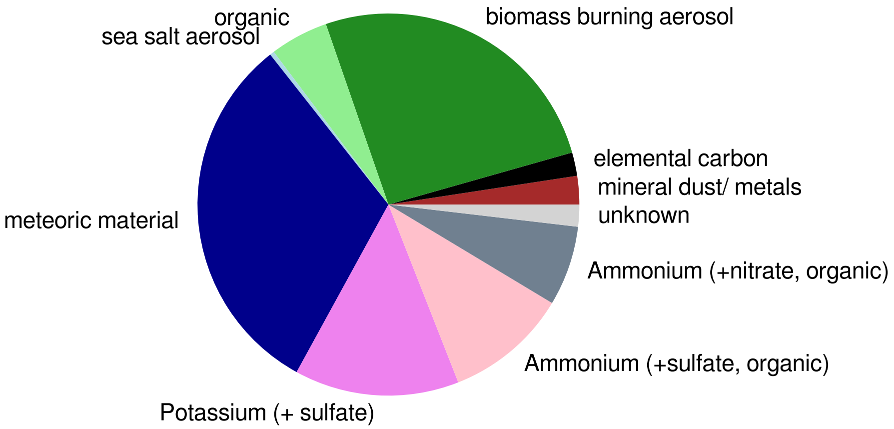

Figure 2. UTLS background particle number type fraction measured by the ALABAMA (size range from 230 to 3000 nm) during the HERA sampling times. The naming of the particle types is based on dominant signals of the the mass spectra.

a loop within and above the anvil cirrus cloud shown as the bright pink area in Fig. 3. Connected to this cloud, which developed close to Brescia, between 15:45 and 16:45 UTC, 95.6 mm of precipitation were measured at a meteorological ground station Astico a Pedescala (Fig. S12), which was located beneath the core of that DCC. Similar precipitation amounts were measured at another nearby weather station (Castana CMT). A significant increase in aerosol particle number concentration was observed in the cloud-free air close to cloud top and identified as cloud-free convective outflow (color code between 15:45 and 16:15 UTC in Fig. 3; see Sec. 3.2.2 for more details). In the following, HALO again moved N into Germany where more DCCs were explored in a descending pattern before landing.

Figure 4a shows the flight track of F15 in terms of pressure as a cross section through the atmosphere, overlaid on ERA5 reanalysis data (relative humidity in green, cloud cover in blue/yellow, isotherms as black lines). Note that the interpolation of the hourly ERA5 data onto the flight track is prone to errors, especially for temporally and spatially confined features such as DCCs. These errors likely produce artifacts like the seemingly vertically broken up cloud structure which do not capture the continuous vertical extent of the developed DCCs during F15. Above the panel, specific flight sections are categorized according to the probed air masses. The color code here and on the flight track in panel a refers to the three HERA filters (for convenience named red, blue, orange) that were sampled and that represent (1) the lower troposphere including the atmospheric boundary layer (Fig. 4a, red lines), (2) in-cloud sections, i.e., convective updrafts and anvil cirrus (Fig. 4a, dark blue lines), and (3) the DCC-influenced UTLS (Fig. 4a, orange lines). In other words, we consider the red filter as representative of aerosol particles and INPs inside the convective inflow, the blue filter as representative of CPRs and INPs inside a DCC, and the orange filter as representative of aerosol particles and INPs in the DCC-outflow-influenced UTLS. The corresponding filter sample location on the flight track is shown in Fig. S11.

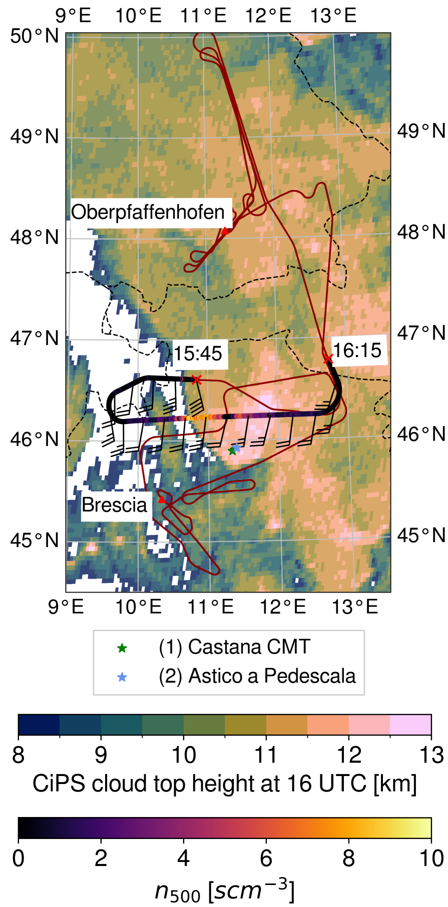

Figure 3. HALO flight track of F15 on the 13th of July 2021 during CIRRUS-HL over Germany, Austria, Switzerland and Italy. The flight track is shown in red. Between 15:45 and 16:15 UTC (positions marked with red crosses) aerosol particle concentrations (n_{500}) are shown color-coded on the flight track, with bright yellow colors indicating high aerosol particle concentrations. Wind barbs displayed in this time section indicate wind speed and direction as measured by HALO research aircraft (half barb mark $5\,m\,s^{-1}$, full barbs $10\,m\,s^{-1}$). The background depicts CiPS cloud top height at 16:00 UTC derived from MSG geostationary satellite images. White areas indicate clear sky conditions. The green and blue stars mark the precipitation measuring weather stations, Castana CMT and Astico a Pedescala, respectively. The flight track is shifted to account for parallax effect of the satellite viewing angle and is shown as it is seen from the satellite point of view. Red triangles mark the start and landing airport Oberpfaffenhofen (EDMO, Germany) and the dive location in Brescia-Montichiari (LIPO, Italy).

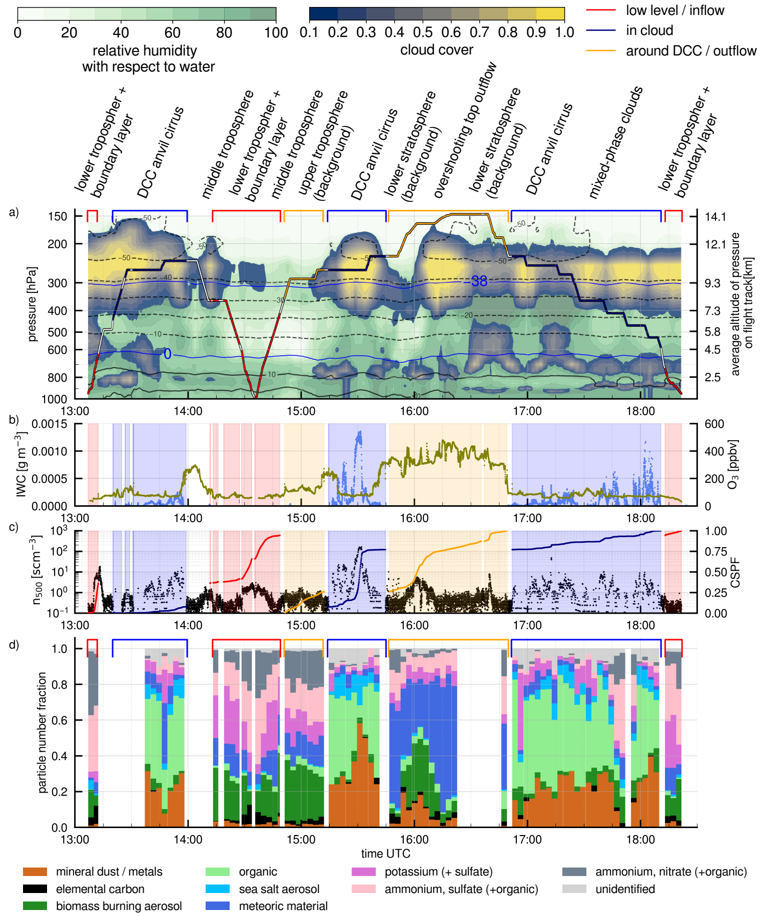

Figure 4. Multi panel time series (UTC) with a flight cross section of F15 in the top panel (a). The colored lines indicate the flight altitude and HERA filter position (orange, blue, red). In the background are ERA5 reanalysis vertical cross section along the flight path. Green contours show relative humidity with respect to liquid water while blue/yellow contours show cloud cover. Isotherms are marked with black lines. While all data is plotted on pressure levels, the right-hand axis indicates the average altitude of the pressure level on the flight track. For more precise height information of the flight track, see Fig.S10c. Panel (b) shows ice water content (IWC, blue) calculated from the Cloud Combination Probe (CCP, De La Torre Castro et al., 2023) and ozone trace gas concentrations (olive green, Zahn et al., 2012). Panel (c) shows concentration of large aerosol particles. The shaded background area marks filter sampling section analogous to the top panel color coding. Outside clouds, measurements of aerosol particle concentrations (d $>$ 500 nm, n_{500}) are shown. Inside cloud (blue shaded areas), CPR concentrations (n_{500}, enrichment factor not accounted for) are shown, measured by the ALABAMA OPC. The colored lines (same sample color coding) corresponds to the right hand axis and indicate the cumulative sampled particle fraction ($CSPF$) of n_{500} for each filter sample. Panel (d) shows the particle number fraction separated into 10 categories using the dominant mass spectra component as measured by the ALABAMA. The clamps above mark the simplified HERA sampling sections. White sections indicate either very low number of detected particles ($< 30\ min^{-1}$) or the ALABAMA not being connected to the same aircraft inlet as HERA.

3.2.2 Sampling conditions and aerosol properties

In the following, we will outline the atmospheric sampling conditions and aerosol particle / CPR properties for each filter on the basis of Fig. 4 before moving on to the discussion of the respective INP spectra in 3.2.3. Hereafter, we will refer to the red filter as "convective inflow", the blue filter as "in-cloud sections", and the orange filter as "convective outflow".

Convective inflow

The convective inflow filter was sampled at the HASI inlet after takeoff and before landing in Oberpfaffenhofen, as well as during a dive over Brescia airport (red lines in Fig. 4a, i.e., in close vicinity of the DCC shown in Fig. 3). Throughout this dive, 52 % of aerosol particles larger than 500 nm (cumulative sampled particle fraction $CSPF$, red line in Fig. 4c) were collected on the filter. Overall, 90 % of aerosol particles larger than 500 nm were sampled below 4 km, making the collected aerosol particles on this filter well representative for the DCC's inflow as well as particles potentially entrained into the DCC in the free troposphere.

During the filter sampling, the ambient temperatures ranged from -30 °C at the highest altitude (8.2 km, 360 hPa; see Fig. 4a) to 23 °C at the surface. Moist, warm, and aerosol-particle-laden air was prevalent in the lower troposphere between 630 hPa and 950 hPa. Colder air with T < 25°C was present between 950 hPa and the surface, likely caused by low-level outflow of nearby DCCs (see Skew-T diagram, SI Fig. 8).

With the exception of a short in-cloud sampling section directly after takeoff at 13:08 UTC, the sample was exclusively collected outside cloud. Operating the HASI inside clouds might lead to artifacts due to hydrometeors shattering at the inlet (Weber et al., 1998). As a result, n_{500} (black dots in Fig.4c) and the $CSPF$ (red line in Fig.4c) might be overestimated to an unknown degree during this short period. Potential effects on the INP results are discussed in Sec. 3.2.3.

Around 6600 mass spectra were recorded with the ALABAMA during the sampling of the convective inflow filter. The aerosol particles consisted mainly of ammonium nitrate (16 %), ammonium sulfate (24 %), potassium and sulfate (19 %) and BBA (19 %, Fig. 4 d, Fig. S6). Sea salt aerosol particles and elemental carbon particles were present but in smaller fractions (4 % and 1 % respectively).

In-cloud sections

The in-cloud filter was sampled at the HALO-CVI in various parts and stages of DCCs (see flight sections marked in blue in Fig. 4a). The first sampling section collected 8 % of the filter's large CPRs (d > 500 nm, see $CSPF$ in Fig. 4c) and was sampled in DCC anvil cirrus at temperatures predominantly between -40 °C and -50 °C (see black isotherms in Fig. 4a). The $CSPF$ in the second section was 70 % , sampling strong DCC updrafts over Italy at 260 hPa and -45 °C ambient temperatures (Fig. 4c). Finally, in the last section, the $CSPF$ was 22 %, sampling in an aged DCC over Germany in both anvil cirrus and the mixed-phase regime in a descending pattern. Here, the ambient temperature ranged from -50 °C to -10 °C. Thus, this sample represents CPRs in DCCs, predominantly collected in updraft regions at ambient temperatures < -40 °C.

Around 4900 mass spectra were recorded during sampling of the in-cloud filter. The chemical composition analysis of the collected CPRs shows that 26 % of the particles consisted of mineral dust, 7 % of sea spray and 35 % of organic material (Fig. 4d, Fig. S6). Mineral dust fractions in anvil cirrus are typically 20–30 %, while values are enhanced up to 54 % within convective core updrafts (see Sec. S4 for more details on mineral dust composition).

Convective outflow

Aerosol particles were collected in the UTLS between 150 and 350 hPa ambient pressure on the convective outflow filter. Ambient temperatures spanned -30 °C to -54 °C, with the majority of sampling below -40 °C (see two orange flight sections and black isotherms, Fig.4a). The filter was sampled almost exclusively outside cloud, except for a short in-cloud sampling section at 14:54 UTC (see IWC in Fig. 4b). Since the $CSPF$ during this in-cloud section was only 1 %, we consider this filter representative for the aerosol particles in the cloud-free air in the DCC outflow.

During the first sampling period from 14:50 to 15:12 UTC, the $CSPF$ was 25 % (orange line in Fig. 4c). Trace gas concentrations remained on typical upper tropospheric levels with carbon monoxide concentrations $< 100\,\mathrm{ppbv}$, methane concentrations $CH_4 < 1.95\,\mathrm{ppmv}$ and ozone concentrations $O_3 < 150\,\mathrm{ppbv}$ (Fig. S10 and Fig.4b), indicating UTLS background conditions and no recent influence of DCCs. Concentrations of aerosol particles larger than 500 nm (n_{500}) were relatively low ($< 1\,\mathrm{scm^{-3}}$) compared to the lower troposphere with n_{500} of ~$2\,\mathrm{scm^{-3}}$. Single-particle mass spectrometry measurements reveal the presence of BBA particles in the upper troposphere at a particle number fraction of around 30 % (Fig. 4 d).

During the second sampling period from 15:46 to 16:49 UTC, aerosol particles were collected above DCCs in the stratosphere with CO $< 50\,\mathrm{ppbv}$, $CH_4 < 1.9\,\mathrm{ppmv}$ and $O_3 > 300\,\mathrm{ppbv}$ during most of the time (Fig. S10 and Fig.4b). For the majority of this sampling period, the stratospheric aerosol was dominated by particles containing meteoric materials dissolved in sulfuric acid (Schneider et al., 2021; Murphy et al., 2014; see Fig. 4 d).

Remarkably, between 15:55 and 16:10 UTC, the water vapor mixing ratio increased from background values of 2.5 ppmv to 4 ppmv (Fig. S10a, the CO concentration slightly increased from $< 50\,\mathrm{ppbv}$ to above 60 ppbv (Fig. S10b), and n_{500} increased from $0.4\,\mathrm{scm^{-3}}$ to up to $10\,\mathrm{scm^{-3}}$(Fig.4c). Variations in trace gas concentrations are connected to variations in aerosol particle number concentrations in such a way that periods of high number concentrations occur contemporaneously with the trace gas composition shifted towards more tropospheric values.

Within this short 15-minute period of high aerosol particle concentrations, the $CSPF$ was 45 % (Fig. 4c). The fractions of mineral dust and BBA type particles are drastically increased to 20 % and 30 %, respectively (Fig. 4d, Fig. S4). A potential pathway for the aerosol particles into the stratosphere is revealed by Cirrus Properties from SEVIRI (CiPS) cloud top height satellite products, showing that the aerosol particles were sampled downwind of a DCC overshooting top (Fig. 3). This overshooting top reached its maximum altitude (12.9 km) about 30 min prior and about 50 km south of the flight track. Due to the limited temporal and spatial resolution of the satellite product, the maximum altitude of the peak height of the overshooting top is likely underestimated, which explains the difference between flight altitude of 13.7 and 12.9 km maximum CiPS cloud top height. The intensity of this DCC is also evident in ground precipitation measurements reaching precipitation rates of $95.6\,\mathrm{mm\,h^{-1}}$ (Fig. S12). Altogether, the most obvious explanation for the high aerosol particle concentrations in the stratosphere between 15:55 and 16:10 UTC is recent upward transport from the troposphere via DCCs into the lower stratosphere, where the aerosol mixed with stratospheric air masses in the convective outflow.

Between 16:15 and 16:45, again typical UTLS background conditions predominated during the sampling of stratospheric aerosol 3 to 4 km above anvil cirrus. In this 30-minute time period, the $CSPF$ was 24 $\%$.

3.2.3 INP spectra

Because of the complicated flight trajectory, and as outlined above, the convective in- and outflow filters contain a modest contribution from UTLS background aerosol, i.e., retrieved INP concentrations are somewhat underestimated and can be regarded as minimum estimates for the in- and outflow INP concentrations. Because all filter samples in this case study feature a different degree of "dilution", i.e., sampling in the low-INP background regime, a direct quantitative comparison of the INP concentrations on the filters is not feasible. However, we can quasi-quantitatively compare the INP concentration of the case study filters to the UTLS background INP concentration. In any case, the shapes of the INP-temperature spectra can be compared to analyze differences in the INP characteristics of the case study filter samples.

Convective inflow

Figure 5c shows that the mean INP concentration of the convective inflow filter (red line) exceeds the UTLS INP background concentration by a factor of 10-50 throughout the temperature range. As stated above, the INP concentration of the filter sample should be regarded as a lower estimate, meaning that the difference between INP concentrations in the convective inflow and the UTLS background is likely even larger than shown in Fig. 5c. As stated above (see Sec. 3.2.2), the short in-cloud sampling period at the HASI described above likely artificially increased aerosol particle number concentrations (see S3 for more details).

INPs active at high temperatures (T_{eff} > -15 °C) are present with at least 0.12 sl^{-1}(red line, Fig. 5). Throughout the investigated temperature range, the lower limit INP concentration of the convective inflow filter is in the range of typical mid-latitude INP concentrations at ground level (Petters and Wright, 2015).

In-cloud sections

Figures 5a and 5b show the activated INP fraction, i.e., the INP concentration normalized by the concentration of aerosol particles / CPRs larger than 500 nm (n_{500}; e.g., Moore et al., 2024). This variable, which also links to a commonly used INP parameterization (DeMott et al., 2010), was chosen for convenient inter-sample comparison of the INP-temperature spectra characteristics. It is preferred over the normalization of INP number to the sampling volume for this case study due to the limitations listed above.

The activated INP fraction of the in-cloud filter (dark blue line in Fig. 5a increases by 2 orders of magnitude within the narrow temperature range of -13.5 °C and -16.5 °C (blue shading in Fig. 5a). The activated INP fraction spectrum slope down to -25 °C is less steep as the INP concentration merely increases by a factor of 10. Sampling of CPRs within DCCs during other CIRRUS-HL research flights resulted in activated INP fraction spectra of similar shape (see light blue curves, Fig. 5 b,

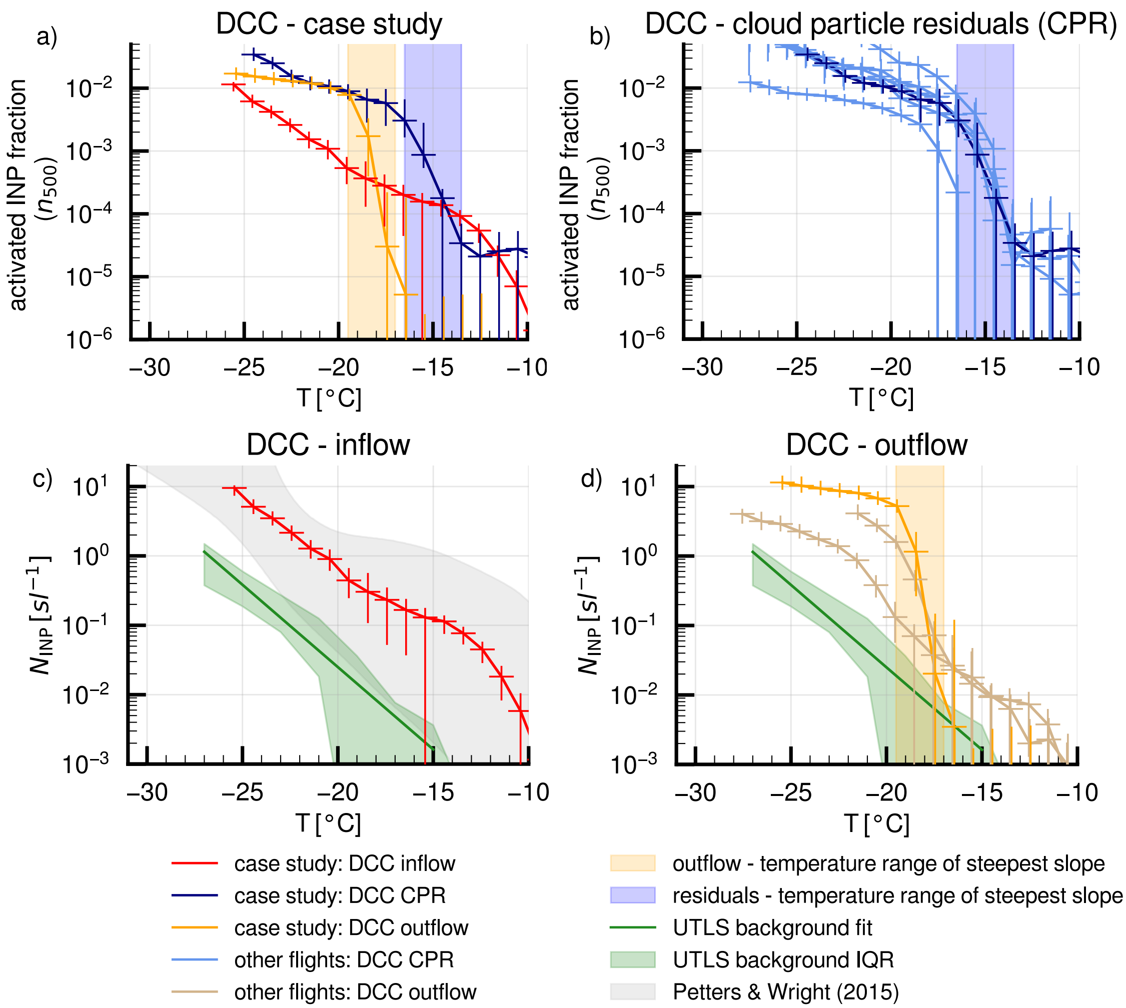

Figure 5. Panel a) shows INP-temperature spectra of flight F15. Red symbols indicate INPs measured in convective inflow, dark blue symbols show INPs from cloud particle residuals (CPR) sampled within DCCs, and orange symbols show INPs partly sampled in convective outflow. To allow convenient comparison between aerosol and cloud residual samples, the activated INP fraction (N_{INP}/N_{500}) is shown. Vertical and horizontal lines mark the 10th to 90th percentiles. Panel b) shows the activated INP fraction of CPR samples from DCCs during other flights of the CIRRUS-HL campaign. Panel c) shows INP concentrations with the convective inflow samples of F15 highlighted. Panel d) shows INP concentrations of DCC outflow samples. In panels a), c) and d), orange and blue shaded areas highlight the temperature range of the steepest slope of the INP spectra in the DCC outflow and in DCC CPR, respectively.

shading same as in panel a), i.e., a steep increase between ~-13.5 and ~-16.5 °C with the fraction of INPs active above -14 °C remaining comparatively small.

Compared to the shape of the activated INP fraction spectrum of the convective inflow filter (red line in Fig. 5a, the in-cloud filter differs significantly, as INPs effective above -15 °C are present in the convective inflow but barely detected in the CPRs. INPs effective below -20 °C are present in both, the convective inflow and the in-cloud filter (Fig. 5a).

Convective outflow

The activated INP fraction spectrum of the convective outflow filter (orange line in Fig. 5a) exhibits a distinct pattern, i.e., a steep increase by at least 2 orders of magnitude between -17 and -19.5 °C (indicated by the orange shading). Between -20 °C to -26 °C, the slope is markedly shallower, increasing only by a factor of 2. This pattern resembles the activated INP fraction spectrum of the in-cloud filter (blue line in Fig. 5). However, the temperature range of the steep increase is shifted towards lower temperatures by 3 to 5 °C for the convective outflow filter. Compared to the activated INP fraction spectrum of the convective inflow filter (red line in Fig. 5a), with its shallow increase over the investigated temperature range, the steep slope and absence of high-temperature INPs above -17 °C for the convective outflow filter are remarkable.

Figure 5d shows the derived INP concentration of the convective outflow filter (orange line) in comparison to the UTLS background INP concentrations (green line). The concentrations of INPs active below -20 °C on the convective outflow filter exceed UTLS background concentrations by at least 2 orders of magnitude. It is also worth mentioning that the convective outflow filter features the highest INP concentrations measured throughout the entire CIRRUS-HL campaign, despite the likely underestimation of the actual INP concentration in the convective outflow regions due to "dilution" with UTLS background aerosol. The observed high INP concentration below -20 °C could indicate a potential enrichment of low-temperature INPs in DCC outflows. However, precise quantification is not feasible here, as it would require more targeted sampling of inflow and outflow of DCCs.

Similarly shaped INP concentration spectra were observed for other filters collected in the vicinity of DCCs at high altitude during other CIRRUS-HL research flights (light brown lines in Fig. 5d). Note that these filters were not exclusively collected in the outflow of DCCs as sampling also occurred in regions with UTLS background concentrations and in clouds. In other words, compared to the presented case study, these samples were collected under less well-defined sampling conditions, likely leading to a smoothing of the INP concentration spectra. Nonetheless, the similarity in shapes of the spectra indicate that the case study's convective outflow filter is not an isolated case.

3.2.4 Vertical transport and segregation of INPs in DCCs

In the following, we propose a mechanism to explain the observed INP characteristics in and around DCCs. We infer that these characteristics are driven by the interplay between ice formation, ice growth, and precipitation in the mixed-phase cloud regime of DCCs, as the range of the steep slope in the INP spectra, which is located between -15 °C and -21 °C, coincides with typical glaciation temperatures of mixed-phase clouds (Yuan et al., 2010; Correia et al., 2021; Lawson et al., 2015; Munawar et al., 2025).

Figure 6 shows a schematic cross section of a DCC. For the description, we follow two types of INPs, precipitating (green) and non-precipitating (purple), on their trajectories through the cloud. In the updraft in the lower part of the DCC, potential INPs

are quickly activated to cloud droplets and experience supercooling (Yuan et al., 2010; Munawar et al., 2025). Following the
345 green trajectories, ice crystals formed through immersion freezing induced by INPs active at high temperatures (> -20 °C) grow fast via the Wegner-Bergeron-Findeisen process (WBF) at ambient temperature spanning around -10 °C to -20 °C (Korolev and Field, 2008). These grown ice crystals collect rime due to their increased surface area and high terminal velocity, which further accelerates the growth process (Laurencin et al., 2022), making them likely to precipitate first from the DCC (DeMott et al., 1998; Stopelli et al., 2015). Consequently, the high-temperature INPs, which initiated the first formation of the ice crystals in
350 the DCC would be efficiently removed from the updraft via precipitation. Such effective removal of high-temperature INPs by precipitation has been observed before (Stopelli et al., 2015; Amato et al., 2015; Pouzet et al., 2017; Els et al., 2019) and explains their absence in the in-cloud and convective outflow filter samples (see Fig. 5a). However, this does not explain why many INPs, initiating freezing at temperatures around -20 °C and below, are present in the outflow of DCCs featuring cloud top temperatures of -50 °C.

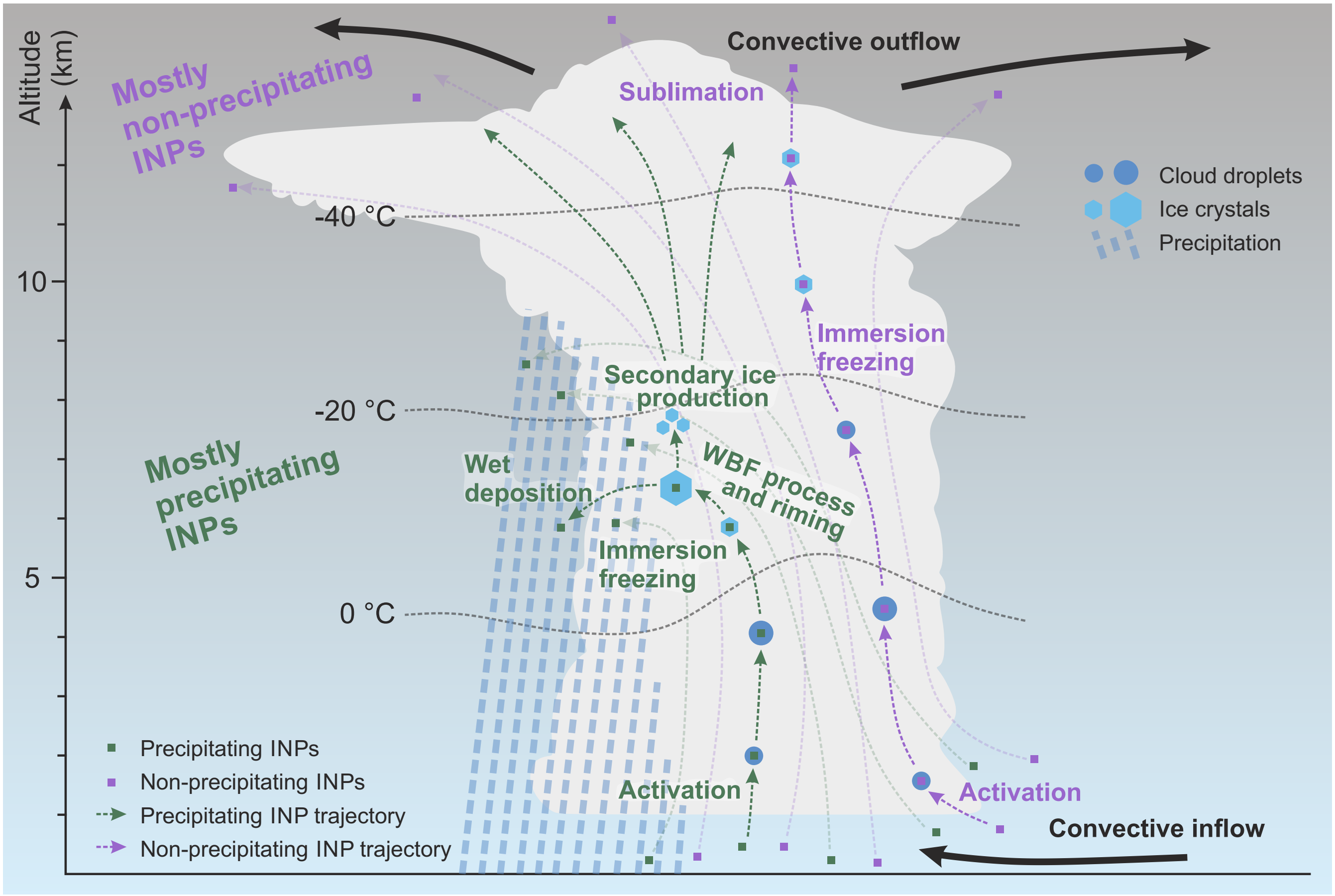

Figure 6. Schematic drawing illustrating the hypothesized selective vertical INP transport in deep convective clouds. WBF: Wegener-Bergeron-Findeisen process.

Following the purple trajectories, low-temperature INPs initiate freezing further up in the DCC at temperatures below -20 °C. In this temperature range, diffusional ice growth is slowed down and riming is suppressed (Muhlbauer and Lohmann, 2009; Xiao et al., 2015; Fan et al., 2017; Lin et al., 2022). Consequently, precipitation formation is less efficient and small ice crystals are effectively transported upward to the anvil and into the outflow (Laurencin et al., 2022), where they sublimate and the contained INPs are released. From there, the INPs will/may sediment to lower altitudes, making them available for primary ice formation in mid- and upper tropospheric clouds. Single particle chemical analysis of CPRs shows an enhanced particle type fraction of mineral dust (Fig. 4 d). Given that mineral dust particles are very efficient INPs (DeMott et al., 2003) in the relevant temperature range of this study, they are the most likely candidate for the observed freezing activity in the in-cloud sample. However, since total INP concentrations are at least 4 orders of magnitude lower than total CPR number concentrations, the bulk CPR composition alone is not sufficient to unambiguously identify the INP subset.

In our case study, the separation between efficient and inefficient precipitation scavenging of INP occurred in a narrow temperature range between -15 °C and -21 °C. One possible explanation for such a narrow temperature range is rapid glaciation within the DCC updraft, caused by riming and secondary ice production (SIP). A variety of different SIP processes have been proposed (Korolev and Leisner, 2020), e.g., ice-ice collisions and fracturing of supercooled large droplets during freezing. The latter has been suggested as a very effective and rapid glaciation process in convective clouds (Lawson et al., 2017). The DCC studied here likely had a cloud base temperature of 15 to 20 °C (see Fig S9 for more details), providing the required preconditions for the formation of supercooled large droplets through collisional coalescence in the form of a sufficiently deep, warm cloud region. Thus, we consider rapid glaciation of the DCC in the temperature range between -15 °C and -21 °C as a likely cause of the observed segregation between high-temperature, precipitating INPs and low-temperature, non-precipitating INPs.

The microphysical pathways governing the interaction between INPs and DCC are inherently complex and remain incompletely understood, in part because they are poorly constrained by in-situ observations within active convection (Lawson et al., 2015; Han et al., 2024). Processes such as SIP, ice growth, aggregation, and phase partitioning of hydrometeors may all contribute to the observed INP characteristics, yet current knowledge does not allow these mechanisms to be quantified or disentangled in great detail for this case study.

4 Summary and conclusion

During the CIRRUS-HL campaign, extensive measurements of aerosol particles, specifically INPs, have been conducted in the upper troposphere and lower stratosphere (UTLS) and in and around deep convection. With this, the present study expands the currently very limited dataset of free tropospheric INP concentrations. To distinguish the effect of deep convection on UTLS INPs, background INP concentrations unaffected by deep convection were quantified throughout the CIRRUS-HL campaign. An exponential curve was fitted to the mean UTLS INP concentrations during CIRRUS-HL as a function of effective temperature between -15 °C and -27 °C with the parameters: a = -0.5465, b = -14.6199 for $N_{\mathrm{INP}} = exp(aT[°\mathrm{C}] + b)$. Previous measurements of free tropospheric background INP concentrations in mid-latitudes at -30 °C align with the fit despite their lower sampling altitude (Lacher et al., 2018).

The effect of deep convection on INPs is showcased utilizing research flight F15, during which INPs were sampled at different stages of deep convective clouds, i.e., in the convective inflow at low levels, within anvil cirrus, and in the convective outflow into the UTLS. In essence, our case study reveals two key findings:

- Deep convective clouds can act as a lifting mechanism for INPs from the boundary layer into the free troposphere. Although not shown in this study, these lifted INPs may influence ice formation in cirrus clouds (Luebke et al., 2016) and, after sedimentation downstream, in mid-level mixed-phase clouds.

- During convective transport, INPs are segregated according to their freezing temperatures, i.e., INPs active at warmer temperatures appear to be preferentially removed by precipitation, while colder-temperature INPs survive transport to the UTLS.

Overall, deep convection may represent an important transport and transformation pathway of INPs from lower altitudes to the free troposphere which should be explicitly resolved or adequately parameterized in atmospheric and climate models.

Ultimately, our results improve our understanding of cloud microphysical processes in deep convective clouds, which are central to extreme weather hazards such as heavy precipitation and hail. However, further observational studies spanning different regions, seasons, and environmental conditions are needed to assess whether the inferred behavior of INPs in convective clouds can be considered universal or generally valid.

Data availability. Processed data from the CIRRUS-HL campaign will become publicly available on the HALO database (http://doi.org/10.17616/R39Q0T) at https://halo-db.pa.op.dlr.de/mission/125 in July 2026. Earlier access to the data is available by contacting the principal investigators of the campaign. Additionally, processed INP data shown in the Figures is available at https://doi.org/10.5281/zenodo.21156567 Schaefer et al. (2026). Data from meteorological ground stations is available at https://meteohub.mistralportal.it/app/maps/observations (Bottazzi et al., 2021).

Author contributions. SG, FS, T. J-W, C.V. designed the research; Jon.S., S.G., H-C.C., Joh.S., S.M., B.W., D.S., J.W., J.M. performed the experiments, Jon.S., H-C.C, B.W., J.W. H.W. and J.M. processed and provided data. Jon.S., S.G., H-C.C., R.S., L.T. and F.S. analyzed the data Jon.S. wrote the paper with contributions from all co-authors

Competing interests. TEXT

The contact author has declared that none of the authors has any competing interests.

Disclaimer. TEXT

Acknowledgements. FS acknowledges funding through DFG within the SPP 1294 (HALO) under grant numbers STR 453/10-1 and STR 453/13-1 (project ID: 316508271, 442648163), JohS and HCC thank Katharina Kaiser (MPIC) for campaign support. HCC acknowledges funding by the DFG through the SPP 1294 (HALO) under grant number SCHN 1138/8-1 (project ID: 442647984). CV acknowledges funding by the DFG through the SPP 1294 (HALO) under grant number VO1504/7-1 and Vo1504/9-1 (project ID:522359172). JM and LT acknowledge funding by the DFG - TRR 301 - Project-ID 428312742. We thank enviscope GmbH for their technical support in the design and operation of HERA on HALO, Conrad Jentzsch, Thomas Conrath and Astrid Hofmann (all TROPOS) for technical support regarding the hardware and software of HERA. We thank Josephine Gundlach and Markus Hartmann (both TROPOS) for support with the immersion-freezing experiments. Chat AI (Doosthosseini et al., 2026) was used for grammar and language optimization. We thank Florian Obersteiner for providing ozone concentration data and Heini Wernli for providing the backward trajectories.

Appendix A: Abbreviations and Acronyms

Table A1. Table of abbreviations and acronyms

Deep convective clouds	DCC
Ice-nucleating particle	INP
free troposphere	FT
CIRRUS in High Latitudes (HALO campaign name)	CIRRUS-HL
High Altitude and Long Range research aircraft (research aircraft)	HALO
Cloud particle residuals	CPR
High-volume flow aerosol particle filter sampler (instrument)	HERA
HALO counter flow virtual impactor	HALO-CVI
HALO sub-micrometer aerosol inlet	HASI
upper troposphere and lower stratosphere	UTLS
Biomass Burning Aerosol	BBA
Leipzig ice nucleation array	LINA
Ice nucleation droplet array	INDA
Aircraft-based laser ablation aerosol mass spectrometer	ALABAMA

References

Amato, P., Joly, M., Schaupp, C., Attard, E., Möhler, O., Morris, C. E., Brunet, Y., and Delort, A.-M.: Survival and ice nucleation activity of bacteria as aerosols in a cloud simulation chamber, Atmospheric Chemistry and Physics, 15, 6455–6465, https://doi.org/10.5194/acp-15-6455-2015, 2015.

Andreae, M. O., Afchine, A., Albrecht, R., Holanda, B. A., Artaxo, P., Barbosa, H. M., Borrmann, S., Cecchini, M. A., Costa, A., Dollner, M., et al.: Aerosol characteristics and particle production in the upper troposphere over the Amazon Basin, Atmospheric Chemistry and Physics, 18, 921–961, https://doi.org/10.5194/acp-18-921-2018, 2018.

Ansmann, A., Tesche, M., Seifert, P., Althausen, D., Engelmann, R., Fruntke, J., Wandinger, U., Mattis, I., and Müller, D.: Evolution of the ice phase in tropical altocumulus: SAMUM lidar observations over Cape Verde, Journal of Geophysical Research: Atmospheres, 114, https://doi.org/10.1029/2008JD011659, 2009.

Barry, K. R., Hill, T. C., Levin, E. J., Twohy, C. H., Moore, K. A., Weller, Z. D., Toohey, D. W., Reeves, M., Campos, T., Geiss, R., et al.: Observations of ice nucleating particles in the free troposphere from Western US wildfires, Journal of Geophysical Research: Atmospheres, 126, e2020JD033 752, https://doi.org/10.1029/2020JD033752, 2021.

Bottazzi, M., Scipione, G., Marras, G. F., Trotta, G., D'Antonio, M., Chiavarini, B., Caroli, C., Montanari, M., Bassini, S., Gascón, E., et al.: The Italian open data meteorological portal: MISTRAL, Meteorological Applications, 28, e2004, https://doi.org/10.1002/met.2004, 2021.

Brands, M., Kamphus, M., Böttger, T., Schneider, J., Drewnick, F., Roth, A., Curtius, J., Voigt, C., Borbon, A., Beekmann, M., et al.: Characterization of a newly developed aircraft-based laser ablation aerosol mass spectrometer (ALABAMA) and first field deployment in urban pollution plumes over Paris during MEGAPOLI 2009, Aerosol Science and Technology, 45, 46–64, https://doi.org/10.1080/02786826.2010.517813, 2011.

Brunner, C., Brem, B. T., Collaud Coen, M., Conen, F., Steinbacher, M., Gysel-Beer, M., and Kanji, Z. A.: The diurnal and seasonal variability of ice-nucleating particles at the High Altitude Station Jungfraujoch (3580 m asl), Switzerland, Atmospheric Chemistry and Physics, 22, 7557–7573, https://doi.org/10.5194/acp-22-7557-2022, 2022.

Bundke, U., Berg, M., Houben, N., Ibrahim, A., Fiebig, M., Tettich, F., Klaus, C., Franke, H., and Petzold, A.: The IAGOS-CORE Aerosol Package: Instrument Design, Operation and Performance for Continuous Measurement Aboard in-Service Aircraft, Tellus B: Chemical and Physical Meteorology, 67, 28 339, https://doi.org/10.3402/tellusb.v67.28339, 2015.

Burrows, S. M., McCluskey, C. S., Cornwell, G., Steinke, I., Zhang, K., Zhao, B., Zawadowicz, M., Raman, A., Kulkarni, G., China, S., et al.: Ice-nucleating particles that impact clouds and climate: Observational and modeling research needs, Reviews of Geophysics, 60, e2021RG000 745, https://doi.org/10.1029/2021RG000745, 2022.

Chen, J., Wu, Z., Augustin-Bauditz, S., Grawe, S., Hartmann, M., Pei, X., Liu, Z., Ji, D., and Wex, H.: Ice-nucleating particle concentrations unaffected by urban air pollution in Beijing, China, Atmospheric Chemistry and Physics, 18, 3523–3539, https://doi.org/10.5194/acp-18-3523-2018, 2018.

Choi, Y.-S., Lindzen, R. S., Ho, C.-H., and Kim, J.: Space observations of cold-cloud phase change, Proceedings of the National Academy of Sciences, 107, 11 211–11 216, https://doi.org/10.1073/pnas.1006241107, 2010.

Clemen, H.-C., Schneider, J., Klimach, T., Helleis, F., Köllner, F., Hünig, A., Rubach, F., Mertes, S., Wex, H., Stratmann, F., et al.: Optimizing the detection, ablation, and ion extraction efficiency of a single-particle laser ablation mass spectrometer for application in environments with low aerosol particle concentrations, Atmospheric Measurement Techniques, 13, 5923–5953, https://doi.org/10.5194/amt-13-5923-2020, 2020.

Conen, F., Einbock, A., Mignani, C., and Hüglin, C.: Measurement report: Ice-nucleating particles active≥- 15° C in free tropospheric air over western Europe, Atmospheric Chemistry and Physics, 22, 3433–3444, https://doi.org/10.5194/acp-22-3433-2022, 2022.

Correia, A. L., Sena, E. T., Silva Dias, M. A., and Koren, I.: Preconditioning, aerosols, and radiation control the temperature of glaciation in Amazonian clouds, Communications earth & environment, 2, 168, https://doi.org/10.1038/s43247-021-00250-3, 2021.

Cziczo, D., Murphy, D., Hudson, P., and Thomson, D.: Single particle measurements of the chemical composition of cirrus ice residue during CRYSTAL-FACE, Journal of Geophysical Research: Atmospheres, 109, https://doi.org/10.1029/2003JD004032, 2004.

De La Torre Castro, E., Jurkat-Witschas, T., Afchine, A., Grewe, V., Hahn, V., Kirschler, S., Krämer, M., Lucke, J., Spelten, N., Wernli, H., Zöger, M., and Voigt, C.: Differences in microphysical properties of cirrus at high and mid-latitudes, Atmospheric Chemistry and Physics, 23, 13 167–13 189, https://doi.org/10.5194/acp-23-13167-2023, 2023.

DeMott, P. J., Rogers, D. C., Kreidenweis, S. M., Chen, Y., Twohy, C. H., Baumgardner, D., Heymsfield, A. J., and Chan, K. R.: The role of heterogeneous freezing nucleation in upper tropospheric clouds: Inferences from SUCCESS, Geophysical Research Letters, 25, 1387–1390, https://doi.org/10.1029/97GL03779, 1998.

DeMott, P. J., Sassen, K., Poellot, M. R., Baumgardner, D., Rogers, D. C., Brooks, S. D., Prenni, A. J., and Kreidenweis, S. M.: African dust aerosols as atmospheric ice nuclei, Geophysical Research Letters, 30, https://doi.org/10.1029/2003GL017410, 2003.

DeMott, P. J., Prenni, A. J., Liu, X., Kreidenweis, S. M., Petters, M. D., Twohy, C. H., Richardson, M., Eidhammer, T., and Rogers, D.: Predicting global atmospheric ice nuclei distributions and their impacts on climate, Proceedings of the National Academy of Sciences, 107, 11 217–11 222, https://doi.org/10.1073/pnas.0910818107, 2010.

Diehl, K. and Grützun, V.: Model simulations with COSMO-SPECS: impact of heterogeneous freezing modes and ice nucleating particle types on ice formation and precipitation in a deep convective cloud, Atmospheric Chemistry and Physics, 18, 3619–3639, https://doi.org/10.5194/acp-18-3619-2018, 2018.

Doosthosseini, A., Decker, J., Nolte, H., and Kunkel, J.: SAIA: A seamless slurm-native solution for HPC-based services, The Journal of Supercomputing, 82, 403, https://doi.org/10.1007/s11227-026-08508-3, 2026.

Eidhammer, T., DeMott, P., Prenni, A., Petters, M., Twohy, C., Rogers, D., Stith, J., Heymsfield, A., Wang, Z., Pratt, K., et al.: Ice initiation by aerosol particles: Measured and predicted ice nuclei concentrations versus measured ice crystal concentrations in an orographic wave cloud, Journal of the Atmospheric Sciences, 67, 2417–2436, https://doi.org/10.1175/2010JAS3266.1, 2010.

Els, N., Larose, C., Baumann-Stanzer, K., Tignat-Perrier, R., Keuschnig, C., Vogel, T. M., and Sattler, B.: Microbial composition in seasonal time series of free tropospheric air and precipitation reveals community separation, Aerobiologia, 35, 671–701, https://doi.org/10.1007/s10453-019-09606-x, 2019.

Fan, J., Leung, L. R., Rosenfeld, D., and DeMott, P. J.: Effects of cloud condensation nuclei and ice nucleating particles on precipitation processes and supercooled liquid in mixed-phase orographic clouds, Atmospheric Chemistry and Physics, 17, 1017–1035, https://doi.org/10.5194/acp-17-1017-2017, 2017.

Gibbons, M., Min, Q., and Fan, J.: Investigating the impacts of Saharan dust on tropical deep convection using spectral bin microphysics, Atmospheric Chemistry and Physics, 18, 12 161–12 184, https://doi.org/10.5194/acp-18-12161-2018, 2018.

Grawe, S., Jentzsch, C., Schaefer, J., Wex, H., Mertes, S., and Stratmann, F.: Next-generation ice-nucleating particle sampling on board aircraft: characterization of the High-volume flow aERosol particle filter sAmpler (HERA), Atmospheric Measurement Techniques, 16, 4551–4570, https://doi.org/10.5194/amt-16-4551-2023, 2023.

Han, C., Hoose, C., and Dürlich, V.: Secondary ice production in simulated deep convective clouds: A sensitivity study, Journal of the Atmospheric Sciences, 81, 903–921, https://doi.org/10.1175/JAS-D-23-0156.1, 2024.

Hartmann, M., Blunier, T., Brügger, S. O., Schmale, J., Schwikowski, M., Vogel, A., Wex, H., and Stratmann, F.: Variation of ice nucleating particles in the European Arctic over the last centuries, Geophysical Research Letters, 46, 4007–4016, https://doi.org/10.1029/2019GL082311, 2019.

Hawker, R. E., Miltenberger, A. K., Johnson, J. S., Wilkinson, J. M., Hill, A. A., Shipway, B. J., Field, P. R., Murray, B. J., and Carslaw, K. S.: Model emulation to understand the joint effects of ice-nucleating particles and secondary ice production on deep convective anvil cirrus, Atmospheric Chemistry and Physics, 21, 17 315–17 343, https://doi.org/10.5194/acp-21-17315-2021, 2021a.

Hawker, R. E., Miltenberger, A. K., Wilkinson, J. M., Hill, A. A., Shipway, B. J., Cui, Z., Cotton, R. J., Carslaw, K. S., Field, P. R., and Murray, B. J.: The temperature dependence of ice-nucleating particle concentrations affects the radiative properties of tropical convective cloud systems, Atmospheric Chemistry and Physics, 21, 5439–5461, https://doi.org/10.5194/acp-21-5439-2021, 2021b.

Hiron, T. and Flossmann, A.: A study of the role of the parameterization of heterogeneous ice nucleation for the modeling of microphysics and precipitation of a convective cloud, Journal of the Atmospheric Sciences, 72, 3322–3339, https://doi.org/10.1175/JAS-D-15-0026.1, 2015.

Jurkat-Witschas, T., Voigt, C., Groß, S., Kaufmann, S., Sauer, D., De la Torre Castro, E., Krämer, M., Schäfler, A., Afchine, A., Attinger, R., et al.: CIRRUS-HL: Picturing High-and Midlatitude Summer Cirrus and Contrail Cirrus above Europe with Airborne Measurements aboard the Research Aircraft HALO, Bulletin of the American Meteorological Society, 106, E2300–E2327, https://doi.org/10.1175/BAMS-D-23-0270.1, 2025.

Korolev, A. and Field, P. R.: The effect of dynamics on mixed-phase clouds: Theoretical considerations, Journal of the Atmospheric Sciences, 65, 66–86, https://doi.org/10.1175/2007JAS2355.1, 2008.

Korolev, A. and Leisner, T.: Review of experimental studies of secondary ice production, Atmospheric Chemistry and Physics, 20, 11 767–11 797, https://doi.org/10.5194/acp-20-11767-2020, 2020.

Lacher, L., DeMott, P. J., Levin, E. J., Suski, K. J., Boose, Y., Zipori, A., Herrmann, E., Bukowiecki, N., Steinbacher, M., Gute, E., et al.: Background free-tropospheric ice nucleating particle concentrations at mixed-phase cloud conditions, Journal of Geophysical Research: Atmospheres, 123, 10–506, https://doi.org/10.1029/2018JD028338, 2018.

Lacher, L., Clemen, H.-C., Shen, X., Mertes, S., Gysel-Beer, M., Moallemi, A., Steinbacher, M., Henne, S., Saathoff, H., Möhler, O., et al.: Sources and nature of ice-nucleating particles in the free troposphere at Jungfraujoch in winter 2017, Atmospheric Chemistry and Physics, 21, 16 925–16 953, https://doi.org/10.5194/acp-21-16925-2021, 2021.

Lacher, L., Adams, M. P., Barry, K., Bertozzi, B., Bingemer, H., Boffo, C., Bras, Y., Büttner, N., Castarede, D., Cziczo, D. J., et al.: The Puy de Dôme ICe Nucleation Intercomparison Campaign (PICNIC): Comparison between online and offline methods in ambient air, EGUsphere, 2023, 1–37, https://doi.org/10.5194/acp-24-2651-2024, 2023.

Laurencin, C. N., Didlake Jr, A. C., Harrington, J. Y., and Jensen, A. A.: Evaluating an Ice Crystal Trajectory Growth (ICTG) Model on a Quasi-Idealized Simulation of a Squall Line, Journal of Advances in Modeling Earth Systems, 14, e2021MS002 764, https://doi.org/10.1029/2021MS002764, 2022.

Lawson, P., Gurganus, C., Woods, S., and Bruintjes, R.: Aircraft observations of cumulus microphysics ranging from the tropics to midlatitudes: Implications for a “new” secondary ice process, Journal of the Atmospheric Sciences, 74, 2899–2920, https://doi.org/10.1175/JAS-D-17-0033.1, 2017.

Lawson, R. P., Woods, S., and Morrison, H.: The microphysics of ice and precipitation development in tropical cumulus clouds, Journal of the Atmospheric Sciences, 72, 2429–2445, https://doi.org/10.1175/JAS-D-14-0274.1, 2015.

Levin, E. J., DeMott, P. J., Suski, K. J., Boose, Y., Hill, T. C., McCluskey, C. S., Schill, G. P., Rocci, K., Al-Mashat, H., Kristensen, L. J., et al.: Characteristics of ice nucleating particles in and around California winter storms, Journal of Geophysical Research: Atmospheres, 124, 11 530–11 551, https://doi.org/10.1029/2019JD030831, 2019.

Li, G., Wieder, J., Pasquier, J. T., Henneberger, J., and Kanji, Z. A.: Predicting atmospheric background number concentration of ice-nucleating particles in the Arctic, Atmospheric Chemistry and Physics, 22, 14 441–14 454, https://doi.org/10.5194/acp-22-14441-2022, 2022.

Lin, Y., Fan, J., Li, P., Leung, L.-y. R., DeMott, P. J., Goldberger, L., Comstock, J., Liu, Y., Jeong, J.-H., and Tomlinson, J.: Modeling impacts of ice-nucleating particles from marine aerosols on mixed-phase orographic clouds during 2015 ACAPEX field campaign, Atmospheric Chemistry and Physics, 22, 6749–6771, https://doi.org/10.5194/acp-22-6749-2022, 2022.

Luebke, A. E., Afchine, A., Costa, A., Grooß, J.-U., Meyer, J., Rolf, C., Spelten, N., Avallone, L. M., Baumgardner, D., and Krämer, M.: The origin of midlatitude ice clouds and the resulting influence on their microphysical properties, Atmospheric Chemistry and Physics, 16, 5793–5809, https://doi.org/10.5194/acp-16-5793-2016, 2016.

Mason, R., Si, M., Chou, C., Irish, V., Dickie, R., Elizondo, P., Wong, R., Brintnell, M., Elsasser, M., Lassar, W., et al.: Size-resolved measurements of ice-nucleating particles at six locations in North America and one in Europe, Atmospheric Chemistry and Physics, 16, 1637–1651, https://doi.org/10.5194/acp-16-1637-2016, 2016.

Mayer, J., Bugliaro, L., Mayer, B., Piontek, D., and Voigt, C.: Bayesian cloud-top phase determination for Meteosat Second Generation, Atmospheric Measurement Techniques, 17, 4015–4039, https://doi.org/10.5194/amt-17-4015-2024, 2024.

McCluskey, C. S., Gettelman, A., Bardeen, C. G., DeMott, P. J., Moore, K. A., Kreidenweis, S. M., Hill, T. C., Barry, K. R., Twohy, C. H., Toohey, D. W., et al.: Simulating Southern Ocean Aerosol and Ice Nucleating Particles in the Community Earth System Model Version 2, Journal of Geophysical Research: Atmospheres, 128, e2022JD036 955, https://doi.org/10.1029/2022JD036955, 2023.

Moore, K. A., Hill, T. C., McCluskey, C. S., Twohy, C. H., Rainwater, B., Toohey, D. W., Sanchez, K. J., Kreidenweis, S. M., and DeMott, P. J.: Characterizing ice nucleating particles over the Southern Ocean using simultaneous aircraft and ship observations, Journal of Geophysical Research: Atmospheres, 129, e2023JD039 543, https://doi.org/10.1029/2023JD039543, 2024.

Muhlbauer, A. and Lohmann, U.: Sensitivity studies of aerosol–cloud interactions in mixed-phase orographic precipitation, Journal of the Atmospheric Sciences, 66, 2517–2538, https://doi.org/10.1175/2009JAS3001.1, 2009.

Mülmenstädt, J., Sourdeval, O., Delanoë, J., and Quaas, J.: Frequency of occurrence of rain from liquid-, mixed-, and ice-phase clouds derived from A-Train satellite retrievals, Geophysical Research Letters, 42, 6502–6509, https://doi.org/10.1002/2015GL064604, 2015.

Munawar, I., Zhu, Y., Wang, M., Rosenfeld, D., Liu, J., and Wang, Y.: The dominant role of aerosol's CCN effect in cloud glaciation, npj Climate and Atmospheric Science, 8, 121, https://doi.org/10.1038/s41612-025-00999-w, 2025.

Murphy, D., Froyd, K., Schwarz, J., and Wilson, J.: Observations of the chemical composition of stratospheric aerosol particles, Quarterly Journal of the Royal Meteorological Society, 140, 1269–1278, https://doi.org/10.1002/qj.2213, 2014.

Ogren, J. A., Heintzenberg, J., and Charlson, R. J.: In-situ sampling of clouds with a droplet to aerosol converter, Geophysical Research Letters, 12, 121–124, https://doi.org/10.1029/GL012i003p00121, 1985.

Petters, M. and Wright, T.: Revisiting ice nucleation from precipitation samples, Geophysical Research Letters, 42, 8758–8766, https://doi.org/10.1002/2015GL065733, 2015.

Pouzet, G., Peghaire, E., Aguès, M., Baray, J.-L., Conen, F., and Amato, P.: Atmospheric processing and variability of biological ice nucleating particles in precipitation at Opme, France, Atmosphere, 8, 229, https://doi.org/10.3390/atmos8110229, 2017.

Roth, A., Schneider, J., Klimach, T., Mertes, S., van Pinxteren, D., Herrmann, H., and Borrmann, S.: Aerosol Properties, Source Identification, and Cloud Processing in Orographic Clouds Measured by Single Particle Mass Spectrometry on a Central European Mountain Site during HCCT-2010, Atmospheric Chemistry and Physics, 16, 505–524, https://doi.org/10.5194/acp-16-505-2016, 2016.

Schaefer, J., Grawe, S., Mertes, S., Wetzel, B., Clemen, H.-C., Schneider, J., Sauer, D., Wolf, J., Henning, S., Pöhlker, M., and Stratmann, F.: INP data of "Upward transport and segregation of ice-nucleating particles in deep convective clouds", https://doi.org/10.5281/zenodo.21156567, 2026.

Schmidt, S., Schneider, J., Klimach, T., Mertes, S., Schenk, L. P., Kupiszewski, P., Curtius, J., and Borrmann, S.: Online Single Particle Analysis of Ice Particle Residuals from Mountain-Top Mixed-Phase Clouds Using Laboratory Derived Particle Type Assignment, Atmospheric Chemistry and Physics, 17, 575–594, https://doi.org/10.5194/acp-17-575-2017, 2017.

Schneider, J., Weigel, R., Klimach, T., Dragoneas, A., Appel, O., Hünig, A., Molleker, S., Köllner, F., Clemen, H.-C., Eppers, O., et al.: Aircraft-based observation of meteoric material in lower-stratospheric aerosol particles between 15 and 68° N, Atmospheric chemistry and physics, 21, 989–1013, https://doi.org/10.5194/acp-21-989-2021, 2021.

Schrod, J., Thomson, E. S., Weber, D., Kossmann, J., Pöhlker, C., Saturno, J., Ditas, F., Artaxo, P., Clouard, V., Saurel, J.-M., et al.: Long-term deposition and condensation ice-nucleating particle measurements from four stations across the globe, Atmospheric Chemistry and Physics, 20, 15 983–16 006, https://doi.org/10.5194/acp-20-15983-2020, 2020.

Stopelli, E., Conen, F., Morris, C. E., Herrmann, E., Bukowiecki, N., and Alewell, C.: Ice nucleation active particles are efficiently removed by precipitating clouds, Scientific reports, 5, 16 433, https://doi.org/10.1038/srep16433, 2015.

Storelvmo, T.: Aerosol effects on climate via mixed-phase and ice clouds, Annual Review of Earth and Planetary Sciences, 45, 199–222, https://doi.org/10.1146/annurev-earth-060115-012240, 2017.

Takeishi, A. and Storelvmo, T.: A study of enhanced heterogeneous ice nucleation in simulated deep convective clouds observed during DC3, Journal of Geophysical Research: Atmospheres, 123, 13–396, https://doi.org/10.1029/2018JD028889, 2018.

Tan, I., Storelvmo, T., and Zelinka, M. D.: Observational constraints on mixed-phase clouds imply higher climate sensitivity, Science, 352, 224–227, https://doi.org/10.1126/science.aad5300, 2016.

Twohy, C. H., DeMott, P. J., Russell, L. M., Toohey, D. W., Rainwater, B., Geiss, R., Sanchez, K. J., Lewis, S., Roberts, G. C., Humphries, R. S., et al.: Cloud-nucleating particles over the Southern Ocean in a changing climate, Earth's Future, 9, e2020EF001 673, https://doi.org/10.1029/2020EF001673, 2021.

Vali, G.: Quantitative evaluation of experimental results an the heterogeneous freezing nucleation of supercooled liquids, Journal of Atmospheric Sciences, 28, 402–409, https://doi.org/10.1175/1520-0469(1971)028<0402:QEOERA>2.0.CO;2, 1971.

Vali, G.: Revisiting the differential freezing nucleus spectra derived from drop-freezing experiments: methods of calculation, applications, and confidence limits, Atmospheric Measurement Techniques, 12, 1219–1231, https://doi.org/10.5194/amt-12-1219-2019, 2019.

Vergara-Temprado, J., Murray, B. J., Wilson, T. W., O'Sullivan, D., Pringle, K. J., Ardon-Dryer, K., Bertram, A. K., Burrows, S. M., Ceburnis, D., DeMott, P. J., et al.: Contribution of feldspar and marine organic aerosols to global ice nucleating particle concentrations, Atmospheric Chemistry and Physics, 17, 3637–3658, https://doi.org/10.5194/acp-17-3637-2017, 2017.

Voigt, C., Schumann, U., Minikin, A., Abdelmonem, A., Afchine, A., Borrmann, S., Boettcher, M., Buchholz, B., Bugliaro, L., Costa, A., et al.: ML-CIRRUS: The airborne experiment on natural cirrus and contrail cirrus with the high-altitude long-range research aircraft HALO, Bulletin of the American Meteorological Society, 98, 271–288, https://doi.org/10.1175/BAMS-D-15-00213.1, 2017.

Voigt, C., Lelieveld, J., Schlager, H., Schneider, J., Curtius, J., Meerkötter, R., Sauer, D., Bugliaro, L., Bohn, B., Crowley, J. N., et al.: Cleaner skies during the COVID-19 lockdown, Bulletin of the American Meteorological Society, 103, E1796–E1827, https://doi.org/10.1175/BAMS-D-21-0012.1, 2022.

Von der Weiden, S.-L., Drewnick, F., and Borrmann, S.: Particle Loss Calculator–a new software tool for the assessment of the performance of aerosol inlet systems, Atmospheric Measurement Techniques, 2, 479–494, https://doi.org/10.5194/amt-2-479-2009, 2009.

Weber, R., Clarke, A., Litchy, M., Li, J., Kok, G., Schillawski, R., and McMurry, P.: Spurious aerosol measurements when sampling from aircraft in the vicinity of clouds, Journal of Geophysical Research: Atmospheres, 103, 28 337–28 346, https://doi.org/10.1029/98JD02086, 1998.

Wieder, J., Mignani, C., Schär, M., Roth, L., Sprenger, M., Henneberger, J., Lohmann, U., Brunner, C., and Kanji, Z. A.: Unveiling atmospheric transport and mixing mechanisms of ice-nucleating particles over the Alps, Atmospheric Chemistry and Physics, 22, 3111–3130, https://doi.org/10.5194/acp-22-3111-2022, 2022.

Xiao, H., Yin, Y., Jin, L., Chen, Q., and Chen, J.: Simulation of the effects of aerosol on mixed-phase orographic clouds using the WRF model with a detailed bin microphysics scheme, Journal of Geophysical Research: Atmospheres, 120, 8345–8358, https://doi.org/10.1002/2014JD022988, 2015.

Yang, Q., Easter, R. C., Campuzano-Jost, P., Jimenez, J. L., Fast, J. D., Ghan, S. J., Wang, H., Berg, L. K., Barth, M. C., Liu, Y., et al.: Aerosol transport and wet scavenging in deep convective clouds: A case study and model evaluation using a multiple passive tracer analysis approach, Journal of Geophysical Research: Atmospheres, 120, 8448–8468, https://doi.org/10.1002/2015JD023647, 2015.

Yin, Y., Chen, Q., Jin, L., Chen, B., Zhu, S., and Zhang, X.: The effects of deep convection on the concentration and size distribution of aerosol particles within the upper troposphere: A case study, Journal of Geophysical Research: Atmospheres, 117, https://doi.org/10.1029/2012JD017827, 2012.

Yuan, T., Martins, J. V., Li, Z., and Remer, L. A.: Estimating glaciation temperature of deep convective clouds with remote sensing data, Geophysical Research Letters, 37, https://doi.org/10.1029/2010GL042753, 2010.

Zahn, A., Weppner, J., Widmann, H., Schlote-Holubek, K., Burger, B., Kühner, T., and Franke, H.: A fast and precise chemiluminescence ozone detector for eddy flux and airborne application, Atmospheric Measurement Techniques, 5, 363–375, https://doi.org/10.5194/amt-5-363-2012, 2012.